Desalination and Water Treatment
www.deswater.com
doi: 10.1080/19443994.2015.1060540

57 (2016) 13549–13560
June

Taylor & Francis
Taylor & Francis Group

Methyl orange adsorption onto simple chemical route synthesized crystalline α-Fe_2O_3 nanoparticles: kinetic, equilibrium isotherm, and neural network modeling

Animesh Debnath[a,b,*], Krishna Deb[a], Kalyan Kumar Chattopadhyay[c], Biswajit Saha[a]

[a]*Department of Physics, National Institute of Technology Agartala, Jirania 799046, West Tripura, India, Tel. +918575015404; email: debnathanimesh@gmail.com (A. Debnath)*
[b]*Department of Civil Engineering, National Institute of Technology Agartala, Jirania 799046, West Tripura, India*
[c]*Thin film and Nanoscience Laboratory, Department of Physics, Jadavpur University, Kolkata 700032, India*

Received 6 April 2015; Accepted 3 June 2015

ABSTRACT

Nanoparticles of α-Fe_2O_3 were synthesized by simple chemical precipitation method and characterized by X-ray diffraction study, scanning electron microscopy, and Fourier transform infrared spectroscopy. Feasibility of as-synthesized nanoparticles was investigated for adsorptive removal of methyl orange (MO) dye from aqueous solution. The effects of various experimental parameters such as solution pH, initial MO concentration, contact time, and α-Fe_2O_3 nanoparticles dose were studied in batch mode. More than 90% removal was reported at pH 2.0 with 30 mg L^{-1} initial MO concentration treated with 1.00 g L^{-1} adsorbent dose. Isotherm study reveals that Langmuir isotherm model is the most efficient one in explaining the process and maximum adsorption capacity as much as 28.90 mg g^{-1} is reported. Kinetic study shows that the adsorption process is best explained by second-order kinetic model confirming the dominancy of chemisorption in the process. Subsequently, the experimental data were modeled by artificial neural network to predict the removal efficiency of MO by α-Fe_2O_3 nanoparticles following conduction of 95 experimental data points. A three-layer feed-forward back-propagation model with Levenberg–Marquardt algorithm was developed which show that the optimal network topology is 4–10–1. Model predicted data shows very good agreement with experimental data set with mean squared error and coefficient of determination (R^2) as 0.00152 and 0.9916, respectively.

Keywords: Artificial neural network; Dye adsorption; Iron oxide nanoparticle; Kinetic and isotherm study

1. Introduction

The natural environment is under serious threat due to rapidly expanding industrialization across the globe. Availability of pure water and sustainable water treatment technique is of great demand from industrial, societal, and environmental point of view. Due to the huge water pollution, increasing attention has been paid to water treatment in the past few decades [1,2]. Wastewater from textile, leather tanning, food processing, paper making, plastic, ceramic, and pharmaceutical industries is a major source of

*Corresponding author.

pollutant dye. Exposure of pollutant dyes in aqueous media is a serious concern to the recent environmental scientists due to their possible carcinogenicity, reproductive toxicity, neurotoxicity, and other skin- and eye-related problems [3–6]. Owing to their complex aromatic structure and synthetic origin, dyes are stable to light, oxidation, and biodegradable process, which provides them a long exposure time in the environment [6,7]. Hence, removal of dyes from industrial effluents has become imperative not only to protect human health but also for the protection of the natural environment [8,9].

Several conventional methods for water treatment are in investigation such as adsorption [10–14], chemical precipitation/oxidation [15–17], ion-exchange [18], and photo-catalytic discoloration [19], while among them, adsorption process becomes most favorable due to its simplicity, high efficiency, adsorbent versatility, low operating cost, and less sludge production [4,20]. The economics and versatility of adsorption process are largely dependent upon the adsorbent material and various low-cost adsorbents, such as hen feather, and egg shell powder, bottom ash, egg shell membrane [6,14,21–23], which have been reported in the literature for removal of dyes as well as heavy metals from wastewater.

One of the recent promising ways to improve the water treatment technology is based on nanoscience, where the materials at the nanoscale appear with profound functionality. Metal oxides have been studied extensively for improving their functionality and exploring their outstanding physical properties in low dimension [24–26]. In this study, highly crystalline α-Fe_2O_3 nanoparticles were synthesized by a very simple chemical precipitation method and its applicability was studied for removal of a pollutant anionic dye of methyl orange (MO) from aqueous media. MO belongs to the azo dyes family and is known to be carcinogenic and mutagenic organic substance, which is widely used in textile, printing, paper manufacturing, pharmaceutical, food industries, and also in research laboratories as an acid–base indicator [27–29]. Iron oxide has relatively high surface areas and surface charges that often regulate free metal and organic matter concentration in soil or water through adsorption reactions. The adsorption process for removal of dye is a nonlinear complex phenomenon, and modeling of such process permits evaluating the effect of each experimental parameter and predicts the removal efficiency with fewer experiments. Artificial neural network (ANN) is an effective tool for mapping nonlinearity between large data set and has been successfully applied for modeling of dye adsorption process [5,30,31].

This study was performed with the following objectives: firstly to synthesize α-Fe_2O_3 nanoparticles by simple chemical precipitation method and to characterize its subsequent physical properties; secondly to explore the effect of different experimental parameters on adsorption capacity of α-Fe_2O_3 nanoparticles for MO removal; and finally to develop a model based on ANN for prediction of removal (%) of MO from aqueous solution.

2. Experimental details

2.1. Materials

All chemicals including ferric chloride hexahydrate ($FeCl_3{\cdot}6H_2O$), NaOH pellets and MO dye ($C_{14}H_{14}N_3SO_3Na$, C.I. 13,025, purity 98%) powder used in this study are of analytical grade and used without further purification. Deionized (DI) water (Millipore, 18 MΩ cm) was used in entire experimental process during the synthesis of adsorbent including MO removal process.

2.2. Synthesis of adsorbent

NaOH was used as precipitating agent for synthesis of adsorbent in this study by employing a simple chemical precipitation method. A homogeneous solution of NaOH was prepared by dissolving 30 g of sodium hydroxide pellets in 1 L DI water at room temperature. Brownish homogenous solution of $FeCl_3$ was prepared by dissolving 40 g of $FeCl_3{\cdot}6H_2O$ in 250 mL of DI water by stirring at room temperature. Thereafter, $FeCl_3$ dissolved solution was mixed slowly to sodium hydroxide solution maintaining pH of the reaction solution at slight alkaline condition (pH: 7.5–8.5) to facilitate the formation of heavy brownish floc of $Fe(OH)_3$. After 60 min, the properly settled floc was separated by filtration and was dried in oven at 85ºC for 8 h. Dried brown particles washed several times with DI water till pH comes close to 7.00, and then, the particles was annealed at 400˚C for 6 h. The chemical reaction of the synthesis process can be represented as follows:

$$FeCl_3 + 3NaOH \rightarrow Fe(OH)_3 + 3NaCl \quad (1)$$

$$2Fe(OH)_3 \rightarrow Fe_2O_3 + 3H_2O \quad (2)$$

Finally the resultant brown product of iron oxide (Fe_2O_3) was grinded manually to make the same in homogenous powder and used as adsorbent for MO adsorption study.

2.3. Characterizations

The physical properties of the prepared Fe_2O_3 powder were studied by different characterizing instruments. X-ray diffraction studies were carried out using an X-ray diffractometer (XRD, Bruker, D–8 Advance) from 20° to 70° with Cu K_α radiation ($\lambda = 1.54178$ °A) for structural investigation. The as-synthesized samples were characterized by field emission scanning electron microscope (FESEM, Hitachi, S–4800) for morphological studies. The Fourier transform infrared (FTIR) spectroscopic measurements of the prepared sample were carried out by employing FTIR (Perkin Elmer).

2.4. Dye removal method

The adsorption studies for removal of MO were performed with batch equilibrium method. A stock solution (100 mg L^{-1}) of MO was prepared by dissolving 0.1 g of MO powder in DI water, and experimental solutions of desired MO concentrations were obtained by successive dilutions of the stock solution with DI water. The batch experiments were carried out by taking 50 mL of MO solution of known concentration in a 125-mL flask. A total of 0.05 g adsorbent were added to each flask, and mixture was agitated at room temperature using a magnetic stirrer with constant speed of 250 rpm for a predetermined time to attain the equilibrium. After adsorption equilibrium was achieved, the supernatant was separated from the adsorbent by centrifugation at 5,000 rpm for 10 min and the amount of MO uptake was monitored spectrophotometrically at the absorbance maximum of MO dye viz. $\lambda_{max} = 464$ nm using a UV–vis–NIR spectrophotometer (Shimadzu UV–3101PC). pH of the aqueous solution was measured by a bench top pH meter (Hach, SensION), and pH of the solution was adjusted to desired values using dilute HCl/NaOH before the addition of adsorbent.

2.5. Definition of the ANN model

Due to effectiveness of ANN to achieve relationship in complex nonlinear data set, the tool has been utilized in this study to investigate the influence of four experimental parameters: solution pH, initial MO concentration (mg L^{-1}), adsorbent dose (g L^{-1}), and contact time (min) on removal (%) of MO as output. A three-layer ANN model with a most commonly used transfer function tan-sigmoid (Eq. (3)) at hidden layer and a linear transfer function purelin (Eq. (4)) at output layer were used. Single hidden layer was used in this study as ANN has the ability to map any input to any output to an arbitrary degree of accuracy with a single hidden layer comprising of suitable large number of neuron [31]. Levenberg–Marquardt (LM) back-propagation algorithm with 1,000 epochs was selected for training of the networks, and a number of neurons were varied from 1 to 30 in the hidden layer.

$$\tan\text{sig}(\text{sum}) = \frac{1 - \exp(-\text{sum})}{1 + \exp(-\text{sum})} \tag{3}$$

$$\text{Purelin}(\text{sum}) = \text{sum} \tag{4}$$

A total of 95 experimental data points were applied for network training to optimize the network topology. Experimental data set was divided randomly into three subsets (70%, 67 data for training; 15%, 14 data for testing; and 15%, 14 data for validation set). Initial MO concentration (5.0–40.0 mg L^{-1}), solution pH (2.0–5.0), adsorbent dose (0.25–1.0 g L^{-1}), and contact time (1–120 min) were utilized as input parameters. All the input and output data were normalized between 0 and 1 to avoid numerical overflow due to very large and small weights before utilizing in ANN [32] according to following expression.

$$X_{norm} = \frac{(X - X_{min})}{(X_{max} - X_{min})} \tag{5}$$

where X is variable, X_{max} is maximum value, and X_{min} is minimum value. The performance of the ANN model was analyzed according to mean squared error (MSE) and coefficient of determination (R^2) which can be represented by (Eqs. (6) and (7)), respectively.

$$\text{MSE} = \frac{1}{N}\sum_{i=1}^{N}\left(|y_{prd,i} - y_{exp,i}|\right)^2 \tag{6}$$

$$R^2 = 1 - \frac{\sum_{i=1}^{N}(y_{prd,i} - y_{exp,i})}{\sum_{i=1}^{N}(y_{prd,i} - y_m)} \tag{7}$$

where $y_{prd,i}$ is the model predicted value, $y_{exp,i}$ is the experimental value, N is the number of data, and y_m is the arithmetic mean of all experimental data.

3. Result and discussions

3.1. Structural characterization of adsorbent

The Fe_2O_3 nanoparticles were studied through X-ray diffraction measurements for structural characterizations. The peaks occurred at 24.2°, 33.3°, 35.8°, 41.0°, 49.5°, 54.2°, 57.6°, 62.5° and 64.2° corresponds to reflections from (0 1 2), (1 0 4), (1 1 0), (1 1 3), (0 2 4),

(1 1 6), (0 1 8), (2 1 4), and (3 0 0) Miller planes. From these studies, it has been observed that the samples are polycrystalline and belong to the alpha (α) phase of iron oxide (JCPDS card number 33–0664) which has rhombohedral structure [33]. The crystallite size has been calculated using X-ray diffraction data by employing Scherrer's equation:

$$D = \frac{0.9\lambda}{\beta \mathrm{Cos}\theta} \tag{8}$$

where D is crystallite size, λ is wavelength of X-ray, β is full width at half maximum in radian, and θ is Bragg angle. The average crystallite size is found to be of the order of 26 nm. This reduced size of the Fe_2O_3 particles increases the effective surface interaction with MO molecule. The surface morphologies of the as-prepared Fe_2O_3 nanoparticles were studied by FESEM. It is observed that powders are of small crystalline grains of Fe_2O_3 with an average grain size of about 60 nm.

3.2. FTIR studies

The FTIR measurements were performed for the Fe_2O_3 nanoparticles, which provide information about the bonding configuration of the compound. Fig. 1 depicts the FTIR spectra of the Fe_2O_3 nanoparticles as obtained from the pellets formed by Fe_2O_3 powders mixed with potassium bromide (KBr). The background correction has been made for infrared light scattering losses in the pellet and for moisture absorbed on the KBr by measuring on the pellet holder with a pellet of KBr only. The mid-infrared, approximately 4,000–400 cm^{-1} range, was selected for this study which corresponds to the fundamental vibrations and associated rotational–vibrational levels. Significant peaks are occurred at wavenumbers 3,429, 1,634, 472, and 555 cm^{-1}. The peak at 3,429 cm^{-1} is due to –OH bond, and the peaks occurring at 472 and 555 cm^{-1} are due to α-Fe_2O_3.

3.3. Effect of pH on adsorption of MO

For adsorption studies, one of the vital factors is its dependence on pH of the solution. On investigating the pH dependence of the MO adsorption onto α-Fe_2O_3 nanoparticles, the removal was found to increase toward acidic pH. A plot showing the variation of MO removal (%) with time at different solution pH (2.0–5.0) is shown in Fig. 2, which depicts that strong acidic condition is favorable for the adsorption of MO. The maximum MO removal (%) ~90% in equilibrium was observed at pH 2.0. Hence, all the further adsorption experiments were conducted at pH 2.0 in this study. The charges of adsorbent and adsorbate play an important role in the process of adsorption. The surface complexation reactions and the electrostatic interactions between MO and the oxide surface are affected by solution pH. The hetero-charge between the adsorbent and adsorbate is in favor of adsorbing reaction. On the other hand, at lower pH, more protons were available to protonate oxides surfaces of adsorbents, which favored the adsorption reaction. pH of the solution thus brings control over

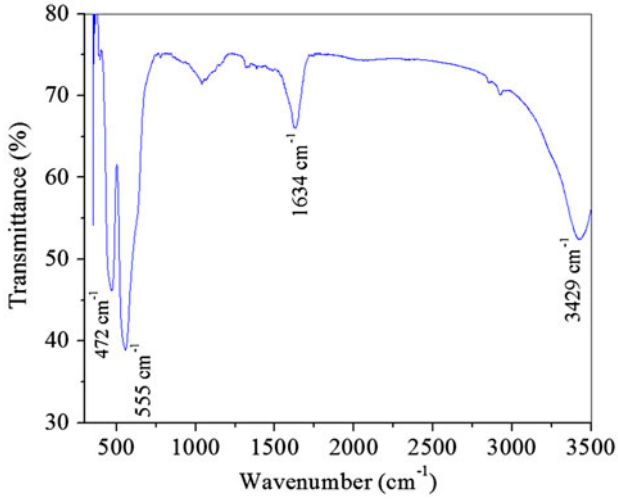

Fig. 1. FTIR spectrum of prepared α-Fe_2O_3 nanoparticles.

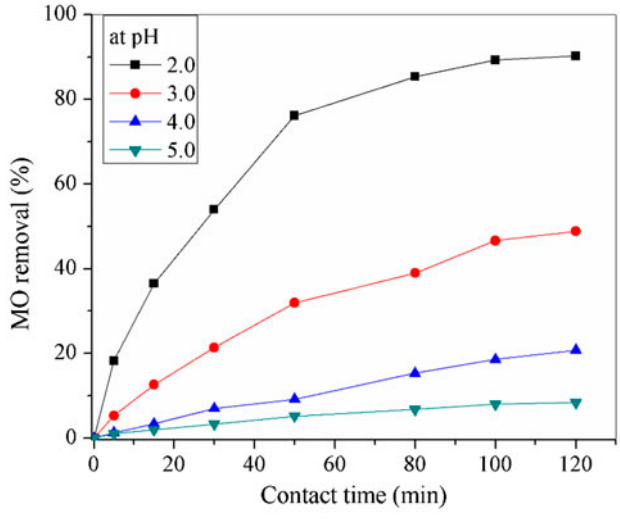

Fig. 2. Plot showing the effect of pH on MO removal (%) with contact time.

the process through the protonation of the adsorbent surface, which plays a role to influence the electrostatic interaction between the adsorbent and MO. Decrease in removal efficiency at higher pH values may be due to the deprotonation of the adsorbent and competitive interaction between hydroxyl ions and anionic part of MO molecule present in the reaction solution.

3.4. Effect of ionic strength of dye and contact time

As the initial adsorbate concentration plays a vital role in the adsorption process, the effect of ionic strength of MO was studied by varying the initial concentration of MO and keeping other reaction conditions unaltered. Fig. 3(a) represents the variation of adsorption capacity as a function of contact time at different initial MO concentration from 10 to 40 mg L^{-1}. At higher concentration of MO, the adsorption capacity was recorded to be high. The higher adsorption capacity at higher MO concentration is because of stronger interaction with the adsorbent at higher ionic concentration of MO.

To study the effect of contact time, MO solution of 30 mg L^{-1} initial concentration was treated by α–Fe_2O_3 nanoparticles with 1.00 g L^{-1} dose for different time. The UV–vis absorption spectra for each of the solution collected for different contact time is shown in Fig. 3(b). Removal of MO was confirmed and estimated from the characteristic absorbance peak at 464 nm with progression of time as shown in UV–vis spectra.

3.5. Effect of adsorbent dose

The effect of adsorbent dose on the adsorption process was studied by keeping other parameters such as initial MO concentration, pH of the solution, and temperature fixed. Fig. 4 depicts the effect of adsorbent dose on MO removal process, where the dose amount of α-Fe_2O_3 nanoparticles was varied from 0.25 to 1.0 g L^{-1}. During this study, the initial concentration of MO was kept constant at 30 mg L^{-1} and the pH of the system was kept at 2.0 at room temperature. It was observed that the percentage removal of MO depends on the adsorbent dose significantly and increases with increasing dose. From the Fig. 4, it is noticed that percentage removal of MO approaches nearing 90% at a dose of 1.0 g L^{-1} with the above-mentioned experimental condition.

3.6. Predictive modeling with ANN

The optimal network topology was attained based on maximum value of R^2 and minimum value of MSE of the training, testing, and validation data set. For optimizing the network, 1–30 numbers of neurons were varied in hidden layer and dependence between the neuron number at hidden layer and corresponding MSE for the LM algorithm was studied (Fig. 5). Table 1 illustrated the variation of R^2 and MSE values with change in the number of neurons (1–30) at hidden layer. It can be suggested from Fig. 5 and Table 1 that the maximum R^2 (0.9916) and minimum MSE (0.00152) were attained using 10 numbers of neurons at hidden layer. A correlation

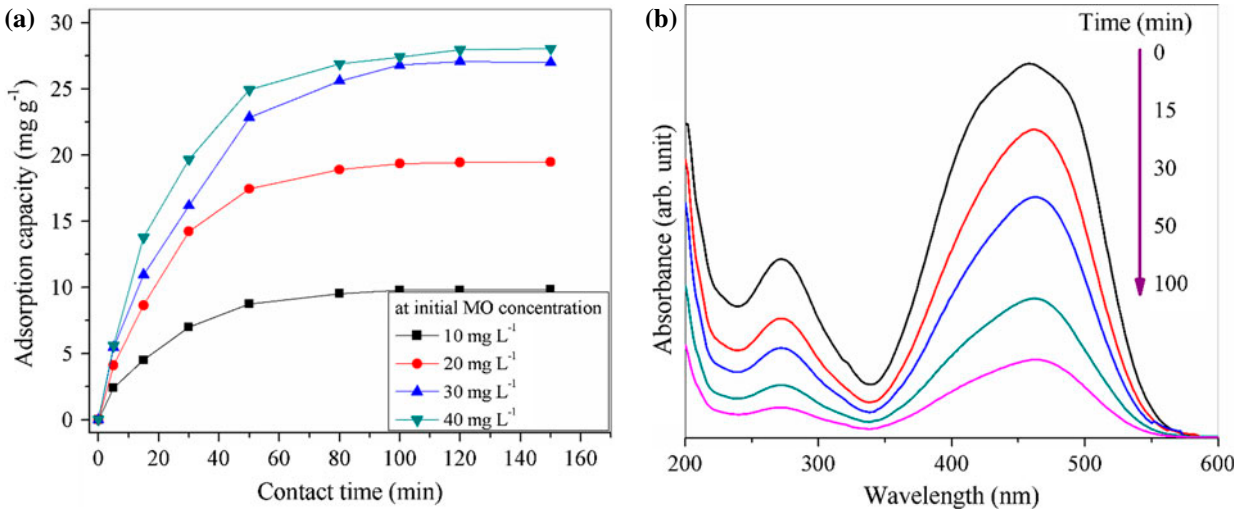

Fig. 3. (a) Adsorption capacity vs. contact time plot for different initial concentration of MO and (b) UV–vis–NIR absorption spectra of MO solutions for different contact time during adsorption onto α-Fe_2O_3 nanoparticles.

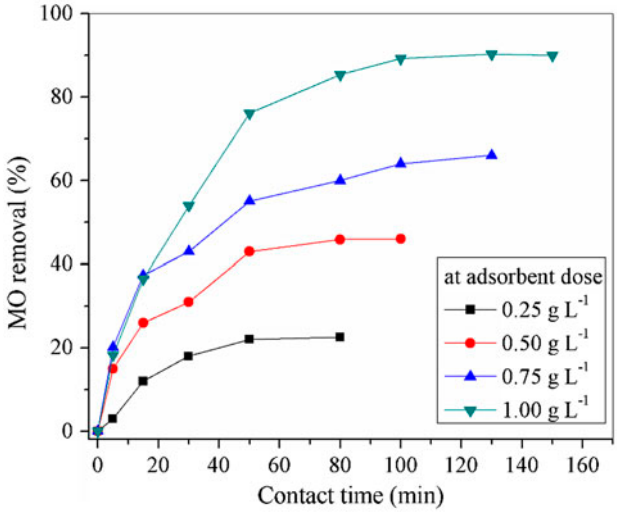

Fig. 4. Plot showing the effect of α-Fe_2O_3 nanoparticles dose on MO removal (%) with contact time.

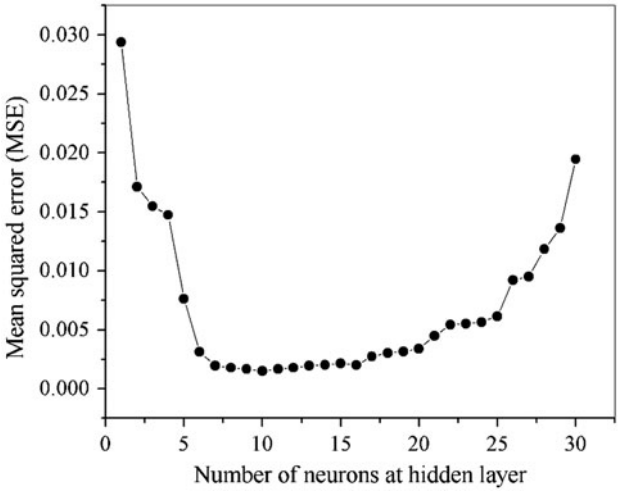

Fig. 5. Plot showing the effect of the number of neurons in the hidden layer on the performance of the neural network.

coefficient of such high value indicates the reliability of the developed ANN model. Hence, the optimal network topology of the ANN model developed in this work involves input layer with 4 neurons, one hidden layer with 10 neurons and one output layer with single neuron and this architecture can be denoted as ANN (4–10–1). The MSE vs. number of epochs for optimal ANN structure is exhibited in Fig. 6, which clearly depicts that training was stopped after 10 epochs as best validation performance was obtained at that epoch. The regression plots of normalized predicted removal data and normalized experimental data for training, testing, validation, and all data are depicted in Fig. 7(a)–(d), respectively, which clearly shows a very good agreement between model predicted and experimental data. The fitness function of the model which correlates the input and output can be defined as follows:

$$\text{ANN output} = \text{Purelin}(\text{LW} \times \tan\text{sig}(\text{IW} \times [x(1); x(2); x(3); x(4)] + b_1) + b_2) \quad (9)$$

where $x(1)$, $x(2)$, $x(3)$, and $x(4)$ represents the inputs, IW and b_1 are the weight and bias of hidden layer, while the LW and b_2 are the weight and bias of output layer. The weight and bias values obtained for optimal network topology are shown in Table 2.

3.7. Sensitivity analysis

Sensitivity analysis was carried out in order to explore the relative importance of each input variable on output by employing connection weight partitioning methodology [31], which is represented in the following equation:

$$V = \frac{\sum_{j=1}^{h}\left[\left(\frac{|\text{IW}_{ij}|}{\sum_{k=1}^{m}|\text{IW}_{kj}|}\right)|\text{LW}_j|\right]}{\sum_{j=1}^{m}\left\{\sum_{j=1}^{h}\left[\left(\frac{|\text{IW}_{ij}|}{\sum_{k=1}^{m}|\text{IW}_{kj}|}\right)\text{LW}_j\right]\right\}} \quad (10)$$

where V is the relative effect of the input variable x, m and h are the neuron numbers in the input and hidden layer, respectively. According to Eq. (10), the relative importance of 4 input parameters was calculated and depicted in Fig. 8. It is clear from figure that solution pH and contact time are the two key variables and initial MO concentration is the least important variable in MO adsorption process.

3.8. Kinetic studies

The kinetic studies are the very essential tools to understand the adsorption mechanism. Four kinetic models such as pseudo-first-order, pseudo-second-order, intra-particle diffusion, and Elovich model were used to investigate the adsorption processes of MO onto α-Fe_2O_3 nanoparticles. The calculated kinetic parameters and correlation coefficients (R^2) for different kinetic models are depicted in Table 3. The pseudo-first-order equation is as follows:

$$\frac{dQ_t}{dt} = k_f(Q_e - Q_t) \quad (11)$$

Table 1
Comparison of number of neurons (1–30) at hidden layer for ANN model development with LM algorithm in terms of MSE and R^2 value

No. of neurons	MSE	R^2	No. of neurons	MSE	R^2
1	0.02939	0.7832	16	0.00202	0.9853
2	0.01712	0.8577	17	0.00274	0.9629
3	0.01547	0.9042	18	0.00302	0.9827
4	0.01473	0.9222	19	0.00317	0.9815
5	0.00763	0.9469	20	0.0034	0.9813
6	0.00312	0.9853	21	0.00448	0.9773
7	0.00197	0.9773	22	0.00543	0.9669
8	0.00178	0.9769	23	0.00552	0.9622
9	0.00166	0.9789	24	0.00567	0.9608
10	0.00152	0.9916	25	0.00615	0.9370
11	0.00166	0.9882	26	0.00923	0.9218
12	0.00178	0.9805	27	0.00952	0.9193
13	0.00197	0.9880	28	0.01182	0.9183
14	0.00203	0.9882	29	0.01362	0.9078
15	0.00217	0.9676	30	0.01945	0.8844

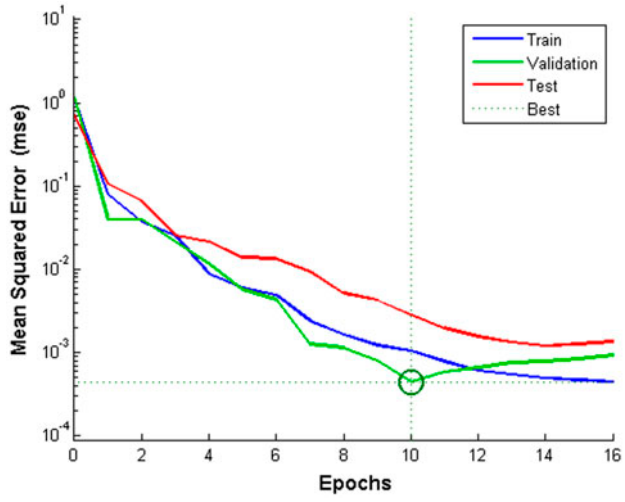

Fig. 6. The MSE vs. number of epochs for optimal network topology of ANN.

where Q_t is the amount of adsorbate adsorbed at time t (mg g^{-1}), Q_e is the adsorption capacity at equilibrium (mg g^{-1}), k_f is the rate constant of pseudo-first-order model (min^{-1}), and t is the time (min). After definite integration by applying the initial conditions $Q_t = 0$ at $t = 0$ and $Q_t = Q_t$ at $t = t$, the equation becomes [34].

$$\log(Q_e - Q_t) = \log Q_e - \frac{k_f}{2.303}t \quad (12)$$

Values of adsorption rate constant (k_f) for MO adsorption on α-Fe_2O_3 nanoparticles can be determined from the linear plot of log ($Q_e - Q_t$) vs. t. From Table 3, it is observed that the values of correlation coefficients (R^2) are in the range of 0.749–0.992. Eq. (13) represents the pseudo-second-order model [35]:

$$\frac{dQ_t}{dt} = k_s(Q_e - Q_t)^2 \quad (13)$$

where k_s is the rate constant of pseudo-second-order model (g mg^{-1} min^{-1}). After integrating Eq. (13) for boundary conditions $Q_t = 0$ at $t = 0$ and $Q_t = Q_t$ at $t = t$, the following form of equation can be obtained:

$$\frac{t}{Q_t} = \frac{1}{k_s Q_e^2} + \frac{1}{Q_e}t \quad (14)$$

The initial sorption rate, h (mg g^{-1} min^{-1}), as $t \to 0$ can be defined as

$$h = k_s Q_e^2 \quad (15)$$

The initial sorption rate (h), the equilibrium adsorption capacity (Q_e), and the pseudo-second-order constant (k_s) can be determined from the slope and intercept of plot of t/Q_t vs. t (Fig. 9), in which the linear plots of the pseudo-second-order model at different initial concentrations of MO (5.0–30.0 mg L^{-1}) are described.

In order to investigate the diffusion mechanisms during adsorption of MO onto α-Fe_2O_3 nanoparticles, widely used intra-particle diffusion model [36] has been applied. An apparent diffusion coefficient can be obtained by fitting the experimental data obtained

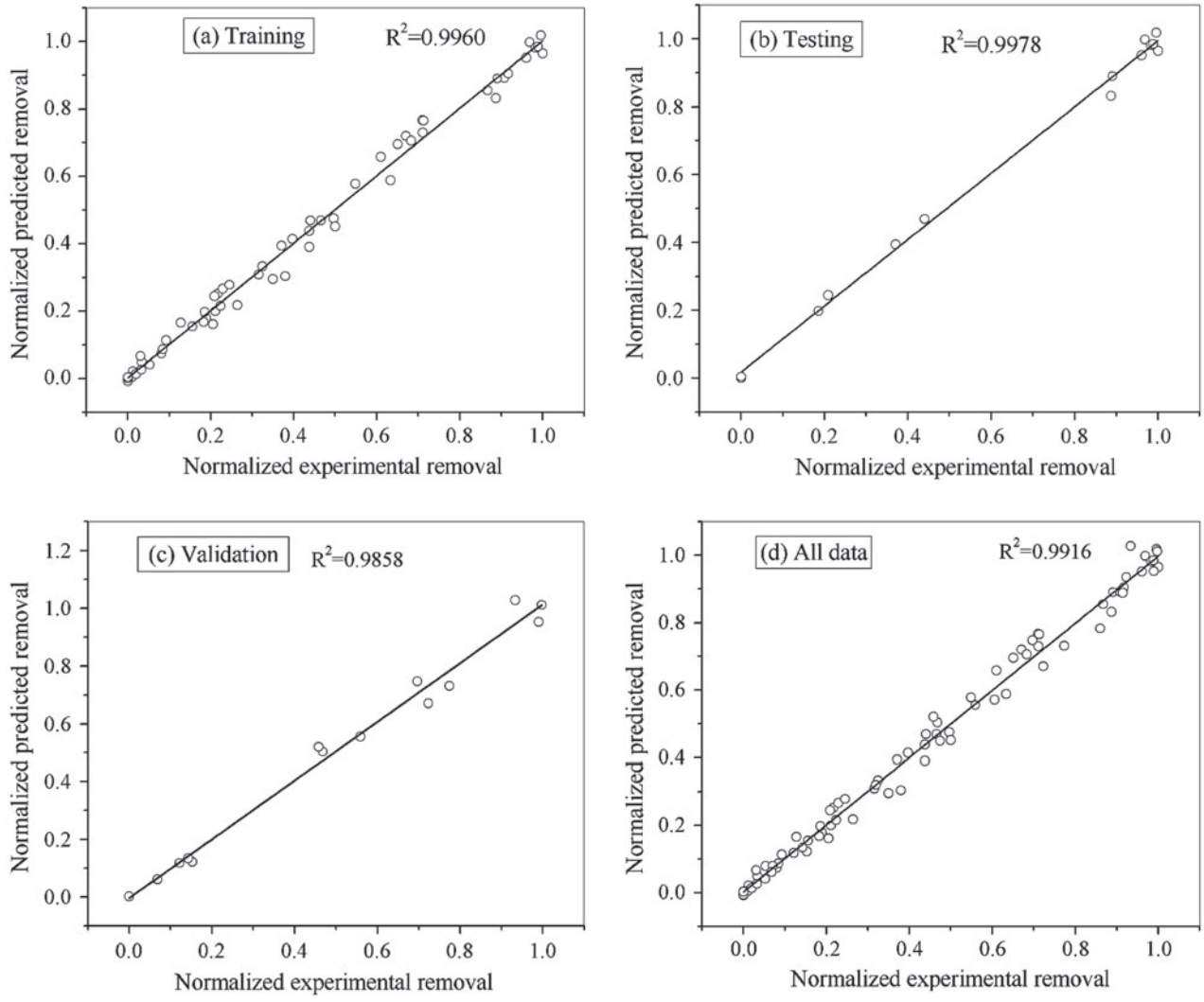

Fig. 7. Scatter plot between normalized model predicted removal and normalized experimental removal (a) for training, (b) for testing, (c) for validation, and (d) all data; for the adsorption of MO onto α-Fe_2O_3 nanoparticles.

from slope of the linear plot of Q_t vs. $t^{1/2}$. The straight line can be represented as follows:

$$Q_t = k_{id} t^{\frac{1}{2}} + c \tag{16}$$

where k_{id} is the intra-particle diffusion rate constant (mg g^{-1} $min^{-1/2}$), and c is the intercept. The intra-particle rate constant (k_{id}) and c values for all initial concentrations of MO are represented in Table 3, which clearly depicts that in the first stage, the order of adsorption rate is higher than that of the second stage. The multilinear fitting of the experimental results in this model indicates that more than one kinetic mechanism is involved in the adsorption process. Elovich equation [37] is another important kinetic model and has been successfully applied for the adsorption of solutes from a liquid solution. The linear form of elovich models is represented as follows:

$$Q_t = \frac{1}{\beta}\ln(\alpha\beta) + \frac{1}{\beta}\ln(t) \tag{17}$$

where α is the initial MO adsorption rate (mmol g^{-1} min^{-1}), and β is the desorption constant (g $mmol^{-1}$) during any one experiment. Plot of Q_t vs. ln (t) leads to a linear relationship that yields the Elovich parameters from its slope and intercept. The

Table 2
The weight and bias values of hidden and output layer for optimally trained ANN network

IW				LW	b_1	b_2
−0.67306	1.7692	1.5879	0.12979	−1.0501	2.5218	−1.0252
3.1044	1.3629	0.079032	0.028599	0.31177	−1.9781	
0.011307	1.147	−3.2817	−0.41013	0.10098	−1.6482	
0.82449	−2.6849	0.19053	0.29329	−0.3056	−1.2317	
−1.3593	0.26416	−0.11038	0.52783	−0.79041	−0.46216	
2.4903	−1.7145	0.70452	0.82587	−0.069398	0.86088	
−1.9067	1.4644	−0.897	−0.74337	0.29153	−2.3249	
−1.1442	1.0229	−2.3279	1.3091	0.25098	−1.1933	
−0.90546	0.32241	−0.11156	−2.1691	−2.1186	−3.7695	
0.47871	1.9296	1.1461	0.6249	−0.3079	2.1823	

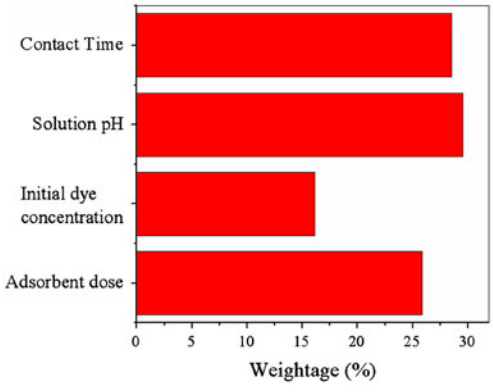

Fig. 8. Plot showing the relative importance of input variables on output variable.

calculated Elovich parameters for MO adsorption on to α-Fe_2O_3 nanoparticles and R^2 values (0.948–0.972) are depicted in Table 3. After comparing the correlation coefficients values of all four kinetic models, it is clear that the second-order model shows highest correlation coefficients (R^2: 0.993 to 0.996) over whole adsorption stage, additionally the closeness of Q_e value calculated from model and experimental data (Q_e(exp)) shows the applicability of this model for analyzing the experimental data. Hence, it can be summarized that the rate determining step may be a chemical adsorption and intra-particle diffusion is also involved in the process.

3.9. Adsorption isotherms

The equilibrium adsorption isotherm models are fundamental tools in describing the interaction mechanism of solutes and adsorbent. Adsorption experiments were conducted at room temperature, and three most commonly used adsorption isotherm models such as Langmuir [38], Freundlich [39] and Temkin [40] were used to fit the equilibrium data obtained from experiments performed with different initial MO concentrations.

The Langmuir equation is applicable to both physical and chemical adsorption, assuming a monomolecular layer adsorption on a uniform surface while ignoring the lateral interactions between the adsorbed molecules [41]. The linear form of the Langmuir isotherm model is described by the following equation:

$$\frac{C_e}{Q_e} = \frac{1}{Q_m b} + \frac{C_e}{Q_m} \tag{18}$$

where Q_m (mg g^{-1}) is the maximum adsorption capacity of the adsorbent, and b (L mg^{-1}) is the Langmuir constant related with the adsorption energy. The favorability of an adsorption process can be described by a dimensionless constant (R_L), which can be obtained from Langmuir model. Generally, R_L value lying in between 1 and 0 indicates a favorable adsorption process. The expression for R_L is given by the following equation:

$$R_L = \frac{1}{1 + bC_0} \tag{19}$$

The logarithmic form of the Freundlich isotherm is expressed by the following equation:

$$\ln Q_e = \ln K_F + \frac{1}{n} \ln C_e \tag{20}$$

where K_F and n are the Freundlich constants related to the adsorption capacity and adsorption intensity, respectively. Values of n, greater than unity, $n > 1$, are indicative of favorable adsorption process.

Table 3
Kinetic parameters obtained from pseudo-first-order, pseudo-second-order, intra-particle, and Elovich kinetic model for MO adsorption onto α–Fe_2O_3 nanoparticles

Models	Equation	Parameters	Initial MO concentration (mg L^{-1})			
			5	10	20	30
First-order kinetic	$\log(Q_e - Q_t) = \log Q_e - \frac{k_f}{2.303}t$	$k_f \times 10^2$	7.89	5.59	5.39	4.97
		Q_e	4.42	11.14	26.46	36.59
		R^2	0.992	0.963	0.952	0.749
Second-order kinetic	$\frac{t}{Q_t} = \frac{1}{k_s Q_e^2} + \frac{1}{Q_e}t$	$k_s \times 10^3$	18.29	5.06	2.26	1.18
		Q_e	5.29	11.12	22.62	32.67
		R^2	0.994	0.996	0.994	0.993
		h	0.512	0.626	1.156	1.260
Intra-particle diffusion	$Q_t = k_{id}t^{\frac{1}{2}} + c$	k_{id1}	0.764	1.230	2.440	3.046
		R^2	0.997	0.994	0.984	0.986
		k_{id2}	0.101	0.359	0.660	1.364
		R^2	0.8174	0.9859	0.982	0.995
		c	3.725	6.247	12.839	13.243
Elovich	$Q_t = \frac{1}{\beta}\ln(\alpha\beta) + \frac{1}{\beta}\ln(t)$	β	0.857	0.423	0.206	0.143
		α	1.023	1.360	2.468	2.786
		R^2	0.948	0.964	0.958	0.972
Experimental value		Q_e(exp)	4.59	9.834	19.472	26.982

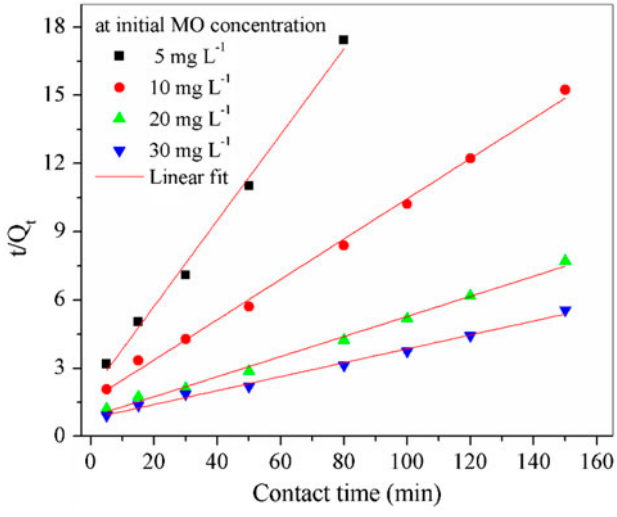

Fig. 9. Plot showing the linear fit of second-order kinetic model at different initial MO concentration.

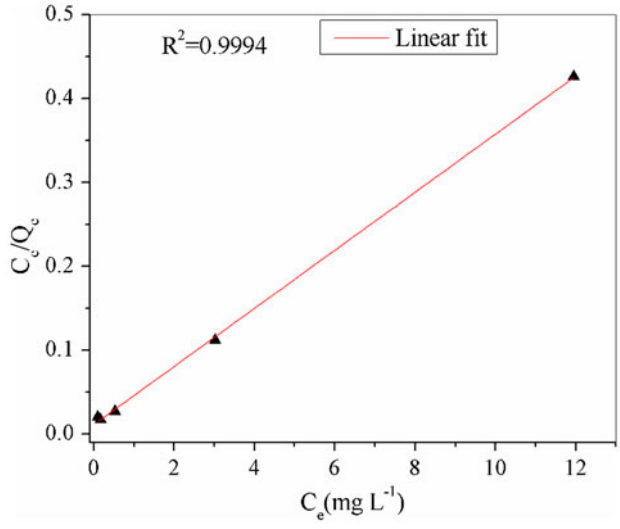

Fig. 10. Plot showing the linear fit of Langmuir adsorption isotherm with experimental results.

Heat of the adsorption process and the interaction between adsorbent and adsorbate can be evaluated by Temkin isotherm, and linear form of the same is expressed by Eq. (21).

$$Q_e = \beta_1 \ln K_T + \beta_1 \ln C_e \quad (21)$$

where β_1 is Temkin constant related to heat of adsorption (J $mole^{-1}$), and K_T is equilibrium binding constant (L mg^{-1}). A plot of Q_e vs. ln C_e enables the determination of isotherm constant β_1 and K_T from the slope and intercept of the straight line, respectively.

The fitting of the experimental data to the three isotherm models showed that the linearity of the Langmuir isotherm model (R^2: 0.999) was higher than that of the Freuindlich (R^2: 0.799) and Temkin (R^2: 0.911) isotherm models. Linear fitting of experimental data in Langmuir isotherm is illustrated in Fig. 10. Isotherm fitting analysis indicates that the adsorption

of MO onto α-Fe_2O_3 nanoparticles is more of monolayer adsorption rather than adsorption on a surface having heterogeneous energy distribution. The maximum adsorption capacity (Q_m) of α-Fe_2O_3 nanoparticles is calculated from Langmuir model as 28.90 mg g^{-1}. Moreover, the values of R_L for all considered initial concentrations of MO were also in the range of 0–1; implying the favorability of the adsorption process.

4. Conclusions

In the context of great demand of industrial wastewater treatment, this article reports an easy synthesis process of crystalline α-Fe_2O_3 nanoparticles. The smaller size and crystalline structure make it as a good adsorbent material. The adsorption of MO molecule was found to depend on the pH of the solution, initial MO concentration, and the dose amount of the adsorbent. From the equilibrium isotherm data analysis, the process of MO removal by α-Fe_2O_3 powder was found to follow Langmuir isotherm model and the kinetic process can be successfully fitted to second-order kinetic model. More than 90% of color removal was achieved within 100 min of contact time with initial concentration of MO 30 mg L^{-1}. The removal efficiency of MO was successfully predicted by applying a three-layer feed-forward neural network model with 10 numbers of neurons in the hidden layer using back-propagation LM algorithm. The scatterplot between experimental removal and model predicted removal shows a very good agreement confirming the accuracy of the developed model with the values of R^2 and MSE as 0.9916 and 0.00152, respectively. Sensitivity analysis shows that input parameters solution pH and contact time are the two key variables for adsorption process of MO by α-Fe_2O_3 nanoparticles. Therefore, it can be concluded that application of ANN model could be an effective way for getting optimal removal of dyes in an automated water treatment process.

Acknowledgement

One of the authors (B. Saha) acknowledges the Department of Science and Technology (DST), Government of India for financial support (Grants order No. SERB/F/7430/2013–14) under Fast Track Young Scientist award scheme.

References

[1] E. Forgacs, T. Cserháti, G. Oros, Removal of synthetic dyes from wastewaters: A review, Environ. Int. 30 (2004) 953–971.

[2] V.K. Gupta, Application of low–cost adsorbents for dye removal–A review, J. Environ. Manage. 90 (2009) 2313–2342.

[3] P. Saha, S. Chowdhury, S. Gupta, I. Kumar, Insight into adsorption equilibrium, kinetics and thermodynamics of Malachite Green onto clayey soil of Indian origin, Chem. Eng. J. 165 (2010) 874–882.

[4] S. Chowdhury, P. Saha, Pseudo-second-order kinetic models for the sorption of malachite green onto *Tamarindus indica* seeds: Comparison of linear and non-linear methods, Desalin. Water Treat. 30 (2011) 229–236.

[5] M. Ghaedi, A. Ansari, F. Bahari, A.M. Ghaedi, A. Vafaei, A hybrid artificial neural network and particle swarm optimization for prediction of removal of hazardous dye brilliant green from aqueous solution using zinc sulfide nanoparticle loaded on activated carbon, Spectrochim. Acta, Part A. 137 (2015) 1004–1015.

[6] J. Mittal, V. Thakur, A. Mittal, Batch removal of hazardous azo dye Bismark Brown R using waste material hen feather, Ecol. Eng. 60 (2013) 249–253.

[7] L. Chen, C. Deng, F. Wu, N. Deng, Decolorization of the azo dye Orange II in a montmorillonite/H_2O_2 system, Desalination 281 (2011) 306–311.

[8] P. Zhang, T. Wang, G. Qian, D. Wu, R.L. Frost, Removal of methyl orange from aqueous solutions through adsorption by calcium aluminate hydrates, J. Colloid Interface Sci. 426 (2014) 44–47.

[9] O. Mohanta, Y.N. Singhbabu, S.K. Giri, D. Dadhich, N.N. Das, R.K. Sahu, Degradation of Congo red pollutants using microwave derived $SrFe_{12}O_{19}$: An efficient magnetic photocatalyst under visible light, J. Alloys Compd. 564 (2013) 78–83.

[10] Q. Ma, F. Shen, X. Lu, W. Bao, H. Ma, Studies on the adsorption behavior of methyl orange from dye wastewater onto activated clay, Desalin. Water Treat. 51 (2013) 3700–3709.

[11] F. Krika, O.E.F. Benlahbib, Removal of methyl orange from aqueous solution via adsorption on cork as a natural and low–coast adsorbent: Equilibrium, kinetic and thermodynamic study of removal process, Desalin. Water Treat. 53 (2015) 3711–3723.

[12] A. Mital, L. Kurup, Column operations for the removal and recovery of a hazardous dye Acid Red–27′ from aqueous solutions, using waste materials-bottom ash and de–oiled soya, Ecol. Environ. Conserv. 12 (2006) 181–186.

[13] G. Sharmaa, M. Naushad, D. Pathania, A. Mittal, G.E. El–desoky, Modification of *Hibiscus cannabinus* fiber by graft copolymerization: Application for dye removal, Desalin. Water Treat. 54 (2015) 3314–3121, doi: 10.1080/19443994.2014.904822.

[14] J. Mittal, D. Jhare, H. Vardhan, A. Mittal, Utilization of bottom ash as a low–cost sorbent for the removal and recovery of a toxic halogen containing dye eosin yellow, Desalin. Water Treat. 52 (2014) 4508–4519.

[15] A. Debnath, R. Thapa, K.K. Chattopadhyay, B. Saha, Spectroscopic studies on interaction of Congo red with Ferric Chloride in aqueous medium for waste water treatment, Sep. Sci. Technol. (in press), doi: 10.1080/01496395.2014.978474.

[16] A. Debnath, S. Chakraborty, Experimental design to optimise colour removal of diazo dye Congo Red

using Zero-Valent Iron, Int. J. Environ. Waste Manage. 11 (2013) 267–288.
[17] R.N. Goyal, A. Kumar, A. Mittal, Oxidation chemistry of adenine and hydroxyadenines at pyrolytic graphite electrodes, J. Chem. Soc., Perkin Trans. 2(9) (1991) 1369–1375.
[18] M. Naushad, A. Mittal, M. Rathore, V. Gupta, Ion-exchange kinetic studies for Cd(II), Co(II), Cu(II), and Pb(II) metal ions over a composite cation exchanger, Desalin. Water Treat. 54 (2015) 2883–2890.
[19] R. Mohammadi, H. Eskandarloo, M. Mohammadi, Application of artificial neural network (ANN) for modeling of dyes decolorization by Sn/Zn–TiO_2 nanoparticles, Desalin. Water Treat. (2014) 1–12, doi: 10.1080/19443994.2014.928237.
[20] A. Mittal, V.K. Gupta, Adsorptive removal and recovery of the azo dye Eriochrome Black T, Toxicol. Environ. Chem. 92 (2010) 1813–1823.
[21] A. Mittal, J. Mittal, Green Chemistry for Dyes Removal from Wastewater: Research Trends and Applications, Scrivener Publishing, Wiley, USA, 2015, pp. 409–457.
[22] H. Daraei, A. Mittal, M. Noorisepehr, J. Mittal, Separation of chromium from water samples using eggshell powder as a low-cost sorbent: Kinetic and thermodynamic studies, Desalin. Water Treat. 53 (2015) 214–220.
[23] H. Daraei, A. Mittal, J. Mittal, H. Kamali, Optimization of Cr(VI) removal onto biosorbent eggshell membrane: Experimental & theoretical approaches, Desalin. Water Treat. 52 (2014) 1307–1315.
[24] B. Saha, N.S. Das, K.K. Chattopadhyay, Combined effect of oxygen deficient point defects and Ni doping in radio frequency magnetron sputtering deposited ZnO thin films, Thin Solid Films 562 (2014) 37–42.
[25] B. Saha, R. Thapa, S. Jana, K.K. Chattopadhyay, Optical and electrical properties of p–type transparent conducting $CuAlO_2$ thin film synthesized by reactive radio frequency magnetron sputtering technique, Indian J. Phys. 84 (2010) 1341–1346.
[26] B. Saha, R. Thapa, N.S. Das, K.K. Chattopadhyay, Quantum size effect on the optical properties of RF magnetron sputtered nanocrystalline cadmium oxide thin films, Int. J. Nanosci. 10 (2011) 713–716.
[27] Y.S. Sohn, Y.R. Smith, M. Misra, V. (Ravi) Subramanian, Electrochemically assisted photocatalytic degradation of methyl orange using anodized titanium dioxide nanotubes, Appl. Catal., B Environ. 84 (2008) 372–378.
[28] M.J. Prival, S.J. Bell, V.D. Mitchell, M.D. Peiperl, V.L. Vaughan, Mutagenicity of benzidine and benzidine–congener dyes and selected monoazo dyes in a modified Salmonella assay, Mutat. Res. Genet. Toxicol. 136 (1984) 33–47.
[29] M. Ghaedi, A.M. Ghaedi, A. Ansari, F. Mohammadi, A. Vafaei, Artificial neural network and particle swarm optimization for removal of methyl orange by gold nanoparticles loaded on activated carbon and Tamarisk, Spectrochim. Acta, Part A. 132 (2014) 639–654.
[30] A. Çelekli, S.S. Birecikligil, F. Geyik, H. Bozkurt, Prediction of removal efficiency of Lanaset Red G on walnut husk using artificial neural network model, Bioresour. Technol. 103 (2012) 64–70.
[31] M. Khajeh, A.R. Golzary, Synthesis of zinc oxide nanoparticles–chitosan for extraction of methyl orange from water samples: Cuckoo optimization algorithm–artificial neural network, Spectrochim. Acta, Part A. 131 (2014) 189–194.
[32] A.K. Giri, R.K. Patel, S.S. Mahapatra, Artificial neural network (ANN) approach for modelling of arsenic (III) biosorption from aqueous solution by living cells of *Bacillus cereus* biomass, Chem. Eng. J. 178 (2011) 15–25.
[33] Q. Hao, S. Liu, X. Yin, Z. Du, M. Zhang, L. Li, Y. Wang, T. Wang, Q. Li, Flexible morphology–controlled synthesis of mesoporous hierarchical α–Fe_2O_3 architectures and their gas–sensing properties, Cryst. Eng. Commun. 13 (2011) 806–812.
[34] S. Lagergren, About the theory of so–called adsorption of soluble substances, Kungliga Svenska Vetenskapsakademiens Handlingar 24 (1898) 1–39.
[35] Y.S. Ho, G. McKay, Pseudo–second order model for sorption processes, Process Biochem. 34 (1999) 451–465.
[36] W.J. Weber, J.C. Morris, Kinetics of adsorption on carbon from solutions, J. Sanit. Eng. Div. Am. Soc. Civ. Eng. 89 (1963) 31–60.
[37] S.H. Chien, W.R. Clayton, Application of elovich equation to the kinetics of phosphate release and sorption on soils, Soil Sci. Soc. Am. J. 44 (1980) 265–268.
[38] I. Langmuir, The constitution and fundamental properties of solids and liquids. Part I. Solids, J. Am. Chem. Soc. 38 (1916) 2221–2295.
[39] H.M.F. Freundlich, Over the adsorption in solution, J. Phys. Chem. 57 (1906) 385–471.
[40] M.I. Temkin, V. Pyzhev, Kinetic of ammonia synthesis on promoted iron, Catalyst Acta Physiochim. URSS 12 (1940) 327–356.
[41] I. Langmuir, The adsorption of gases on plane surfaces of glass, mica and platinum, J. Am. Chem. Soc. 40 (1918) 1361–1403.